Nuclear magnetic resonance imaging and velocimetry of Fano flow

Nuclear magnetic resonance imaging and velocimetry of Fano flow

P T Callaghan[1,3] and Y Xia[1,2]

[1] MacDiarmid Institute for Advanced Materials and Nanotechnology, School of Chemical and
Physical Sciences, Victoria University of Wellington, New Zealand
[2] Department of Physics, Oakland University, Rochester, MI 48309, USA

Abstract
We present an analytic model for the velocity field within a tubeless siphon
(Fano flow), based on a simple differential equation in which extensional, shear
and gravitational pressure gradient forces are balanced. The role of surface
tension in determining boundary conditions for the flow is considered. The
analysis is applied to nuclear magnetic resonance velocimetry data (Xia and
Callaghan 2003 *J. Magn. Reson.* **16** 365) on a 1.2 mm diameter column of
0.5%, 8×10^6 Da polyethylene oxide in water.

(Some figures in this article are in colour only in the electronic version)

1. Introduction

The 'tubeless siphon' effect was first described by Fano [2] in 1908. The phenomenon arises
when the tip of a narrow pipe attached to a vacuum source, or pump, is dipped into an elastic
liquid to establish an upwards flow, the tip then being subsequently lifted above the liquid
surface, drawing with it a filament of fluid which maintains a constant flow rate from the
liquid reservoir to the pipe. The 'Fano effect' is most clearly demonstrated in fluids where the
ratio of extensional to shear viscosities (the Trouton ratio) is high. It is commonly observed
in solutions with high polymer content where a combination of entanglement effects and
intra-chain configurational entropy lead to large elastic stresses. An early observation of the
phenomenology of elastic liquids is a description of the drawing of bitumen onto the deck of
a boat, noted in the *Annals of Tacitus* in around 100 AD.

Figure 1 depicts the essential details of the flow. A pipe, of inner diameter a_0, is used
to draw in the free fluid, the tube entrance being at a height h above the surface of the fluid
reservoir. In Fano flow, the diameter of the free fluid column, $a(z)$, is observed to increase with
distance below the pipe entrance. The physics of the tubeless siphon effect can be expressed

---

[3] Author to whom any correspondence should be addressed.
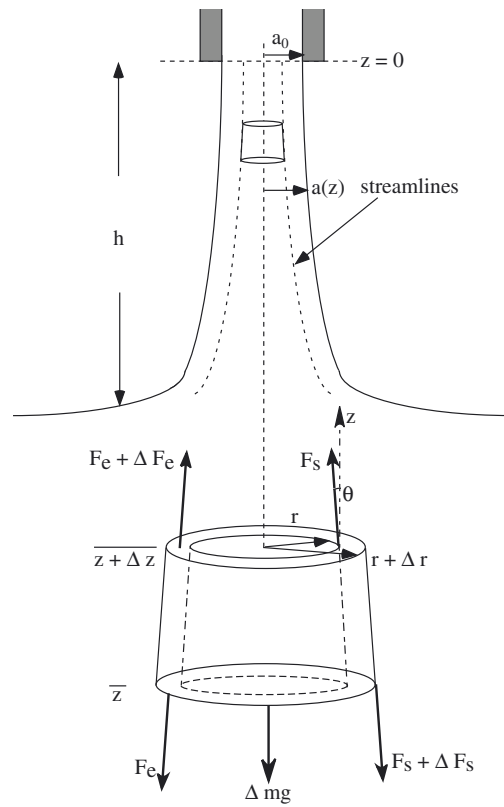
Figure 1. A schematic diagram depicting Fano flow in a tubeless siphon. The lower part shows an annulus of fluid bounded by streamlines. Vectors show forces arising from shear stress (F_s), extensional stress (F_e) and weight (Δmg).

in simple terms via the facility of the siphon to maintain a uniaxial extensional flow. This allows the normal stress associated with the extensional strain rate to balance the weight of the column. Writing the extensional strain rate as $\dot{\epsilon} = \partial v_z / \partial z$, where z defines the vertical axis, the extensional viscosity, $\bar{\eta}_e$, is defined by [3]

$$\sigma_{zz} - \sigma_{xx} = \bar{\eta}_e \dot{\epsilon} \tag{1}$$

where σ_{zz} and σ_{xx} are diagonal elements of the Cartesian stress tensor. Note that a normal stress difference is used so that isotropic pressure terms are removed. Since we may use the transverse diagonal element of the stress tensor, σ_{xx}, as a reference for the isotropic pressure, the difference $\sigma_{zz} - \sigma_{xx}$ is the quantity of interest in determining any net force along the z axis exerted on any surface normal to z.

In principle therefore, the Fano siphon can be used as a means of determining the extensional viscosity, $\bar{\eta}_e$. In its simplest form, the method relies on a measurement of the volume flow rate, Q, along with the Fano column profile, $a(z)$ [4–7]. Provided that one assumes a homogeneous flow (i.e. v_z independent of radius r within the column), the local velocity v_z, and hence the local extension rate $\partial v_z / \partial z$, may be calculated. A measurement of the flow induced vertical force experienced by the pipe then allows the normal stress to be determined [7], thus leading to an estimate of $\bar{\eta}_e$. Measurements of $\bar{\eta}_e$ in a range of polymer solutions have been performed by a number of authors [4, 5, 8–11], in some cases with siphon

heights extending to 20 cm in length. One of the particular advantages of the tubeless siphon, as a means of measuring $\bar{\eta}_e$, is that it operates, in an Eulerian sense, under steady state flow conditions, like the opposed jet device [12] and the four-roll mill [13, 14]. However, as is always the case in extensional flow, the motion of each element of the fluid is transient in a Lagrangian sense.

One simple method for estimating $\bar{\eta}_e$ is to simply observe the maximum length of a stable Fano column at any given flow rate [10]. However, the factors which determine the maximum height are not clear. Chao and Williams [10] have suggested that this height may be associated with a nominal minimum value of $\dot{\epsilon}$, although they acknowledge that this value may vary between different fluids. Clearly the physics of the siphon near its base becomes complex. First, there is a noticeable inflection in $a(z)$ at the base where 'bulging' is observed [5]. Second, most theoretical treatments fail near the base, a failure which is exacerbated by the sudden increase in radius.

It has been shown [6] that the assumption of zero shear in the siphon column can only be justified if the column diameter is constant, i.e. $\partial a(z)/\partial z = 0$, a condition which violates volume conservation given that v_z must vary with height to sustain extensional flow. However, observations of $a(z)$ behaviour in Fano flow suggest that $\partial a(z)/\partial z$ may be sufficiently small at the top of the column that the assumption can be justified [6] in this region. Paradoxically, it is at the top of the column where shear is most likely to occur, since shear stresses arising from a non-slip boundary condition in the inlet pipe will certainly lead to shear in the fluid at the entrance. To satisfy this boundary condition shear must persist for some distance down the column. In an important experiment, Matthys [11] carried out a flow visualization measurement in a Fano column using a photochromic dye marker. Those measurements clearly indicated the existence of shear in the column, and that the shear rate increased with proximity to the pipe entrance.

While precise and convenient to apply, optical velocimetry suffers from some disadvantages. Refraction effects can lead to distortion at the liquid/air interface making surface determinations of velocity difficult. Equally, distortion may be a problem in regions of high surface curvature, such as near the base of the column. And of course, opaque materials do not lend themselves to optical study. By contrast NMR velocimetry, while more complex and specialized, enables the study of opaque fluids and does not need correction for local refractive distortion effects. This method has the potential to provide detailed non-invasive insight regarding absolute velocities in the column and thereby presents an opportunity to make a study of the entire flow field. Furthermore, NMR lends itself to a number of localized spectroscopic studies in which molecular organization and dynamics can be mapped at different parts of the flow. It is for these reasons that we have applied the technique of NMR microscopy to the study of the velocity field within a Fano flow column. It should be noted that many NMR measurements rely on signal averaging over many seconds. While other methods of measuring extensional viscosity in liquids, such as filament stretching rheometry [15], may be more precise than the Fano flow approach discussed here, the Eulerian steady state feature of Fano flow permits long time signal averaging at a particular point within the velocity field, thus making it particularly suited to NMR study.

In this paper we present results obtained on an elastic solution with high polymer content dissolved in water. We will show, conclusively, that shear effects are not only important but that they dominate Fano flow in the upper region of the column. To that end we have reworked the theory to incorporate shear effects in an explicit manner. We present here a simple ansatz which permits an analytic solution for $v_z(r, t)$ which is valid in that upper column region. We show that it is possible to use velocimetry measurements to determine the ratio $\bar{\eta}_e/\eta$ in the absence of any knowledge of the normal force. It would be interesting to compare the extensional

viscosity obtained by comparison with the known shear viscosity, with that determined using a traditional Fano column approach by direct measurements of extensional stress. Unfortunately the latter measurement is not easily achieved in the geometry required for nuclear magnetic resonance imaging studies.

2. Theory

In attempting to obtain analytic expressions for the longitudinal velocity field, $v_z(r, z)$, within a tubeless siphon, we utilize the simple force balance indicated in the lower part of figure 1. Here we consider an annulus of height Δz and of inner and outer radii r and $r + \Delta r$ respectively, defined by streamlines of the fluid within the siphon. Extensional and shear forces are taken to be parallel to the column streamlines, but, consistent with observations, we take the streamline inclination angle, $\theta = \partial a(z)/\partial z$, to be sufficiently small that $\cos(\theta) \approx 1$. Balancing the forces arising from the extensional stress, $\bar{\eta}_e \partial v_z(r, z)/\partial z$, the shear stress, $\eta \partial v_z(r, z)/\partial r$, and the gravitational pressure gradient, ρg, we obtain

$$\bar{\eta}_e \frac{\partial^2 v_z(r, z)}{\partial z^2} + \eta \frac{1}{r} \frac{\partial}{\partial r} r \frac{\partial v_z(r, z)}{\partial r} = \rho g. \tag{2}$$

Clearly, any solution to equation (2) must satisfy continuity by conserving the rate of volume flow up the column. Because equation (2) implies that the mean value of v_z varies with height, z, the column will have a radius, $a(z)$, which in turn depends on z.

A trivial solution to equation (2) is given by $v_z(r, z) = B + C(z + h)^2$. Such a solution however does not allow for the existence of shear $(\partial v_z/\partial r)$ in the flow field and thus cannot satisfy the boundary condition for $v_z(r, z)$ at the pipe entrance. For the moment, it is instructive to consider the case where the column radius a is constant and for which a naive 'solution' to equation (2) is given by

$$v_z(r, z) = A J_0(\alpha r) \exp(-kz) + B + C(z + h)^2 \tag{3}$$

where A, B and h are constants, $J_0(\alpha r)$ is the zeroth-order cylindrical Bessel function,

$$C = \frac{\rho g}{2\bar{\eta}_e} \tag{4}$$

and

$$k^2 = \frac{\eta}{\bar{\eta}_e} \alpha^2. \tag{5}$$

We are therefore tempted to seek an approximate (first-order) solution of the form

$$v_z(r, z) = A J_0(\alpha(z)r) \exp(-k(z)z) + B + C(z + h)^2. \tag{6}$$

We shall seek to justify our simple ansatz by verifying that we may neglect the residual error terms in equation (6) generated by the height dependence of α and k. For the moment however, consider the behaviour at the column surface where $r = a(z)$. In the absence of surface tension effects, a zero-shear boundary condition will apply, whence $J_0'(\alpha a) \sim J_1(\alpha a) = 0$, i.e. assuming the first root of J_1, $\alpha(z) = 3.8317/a(z)$. Since $\int_0^a 2\pi r J_0(\alpha r) \, dr \sim J_1(\alpha a)$, only the second two terms in equation (6) contribute to the rate of volume flow, Q, up the column. Hence, applying mass conservation,

$$B = \frac{Q}{\pi a_0^2} - Ch^2 \tag{7}$$

and

$$a(z)^2 = \frac{Q}{\pi [B + C(z + h)^2]} \tag{8}$$

where $a_0 = a(0)$. Note that in this formulation, the origin of z is taken at the tube entrance so z is negative within the column. For $|z| < h$, the velocity averaged across the column decreases, while the column radius increases with distance below the tube entrance, consistent with observations of Fano flow. For $|z| > h$ however, the mean velocity starts to rise again, with the column radius decreasing. Thus we view this transition to unphysical behaviour as defining the maximum vertical extent of the column and set h equal to the column height.

Note that A will be determined by the boundary conditions associated with the entrance to the pipe. For example, if there is no slip at the boundary, $A = Q/\pi a_0^2 J_0(\alpha a_0)$. However, the non-slip condition is unlikely to be found until the fluid has travelled some distance along the pipe, at least of the order of one or two tube diameters. Given that the velocity profile at $z = 0$ will depend on details of the fluid–wall interaction, we will regard A as a boundary condition parameter to be set subsequent to a measurement of $v_z(r, 0)$.

Given these various constraints, the analytic expression, equation (6), has only one free fitting parameter, namely the extensional viscosity, $\bar{\eta}_e$. In the experimental section of this paper we shall show how velocimetry can be used to estimate this important material property.

2.1. The influence of surface tension

The boundary condition $J_1(\alpha(z)a) = 0$ applies only where there is no surface tension. For $\gamma > 0$, a finite shear stress is needed at the outer surface to provide a force balance, γ being the usual force per unit length on the fluid/air surface. Utilizing figure 1 and allowing for surface tension effects at the outer surface, it is straightforward to show that

$$\left. \frac{\partial v_z}{\partial r} \right|_{r=a} = \frac{\gamma}{\eta a(z)} \frac{\partial a(z)}{\partial z}. \tag{9}$$

From equation (6) we find

$$\left. \frac{\partial v_z}{\partial r} \right|_{r=a} = -\alpha A J_1(\alpha a) \exp(-kz) \tag{10}$$

so J_1 at the column surface is non-zero and the volume flow rate has an additional contribution:

$$Q = \frac{2\pi}{\alpha^2} \left| -\frac{\gamma}{\eta} \frac{\partial a(z)}{\partial z} \right| + [B + C(z + h)^2]\pi a^2. \tag{11}$$

We shall show in the discussion section that for the fluid used in this work, the surface tension term comprises a small effect over most of the column, and we shall accordingly neglect it.

2.2. Residual errors in equation (6)

The use of equation (6) as a solution to equation (2) under the requirements of continuity can only be justified if the additional terms associated with the z dependence of α and k can be neglected to first order. In order to appreciate the importance of those terms, it is helpful to consider the relative magnitudes of the extension, shear and gravitational terms in equation (2). The first two terms exceed the third by the ratio $\frac{\eta \times 3.8^2 Q \exp(-kz)}{\pi a^4 \rho g}$. Near the pipe entrance, where $\exp(-kz) \approx 1$, this factor is large. It corresponds to the ratio of the pressure difference needed to cause a flow Q in a pipe of the same diameter as the tubeless column to the gravitational pressure drop along the column. For the fluid used in this work, with a shear viscosity of the order of 0.1 Pa s, the factor is around 20. Thus most of the extensional stress near the pipe entrance is used to balance the shear stress associated with the shear deformation arising from flow near the entry. Further down the tubeless column, where $\exp(-kz) \ll 1$ and the shear deformation damps out, gravitational effects begin to dominate the flow.
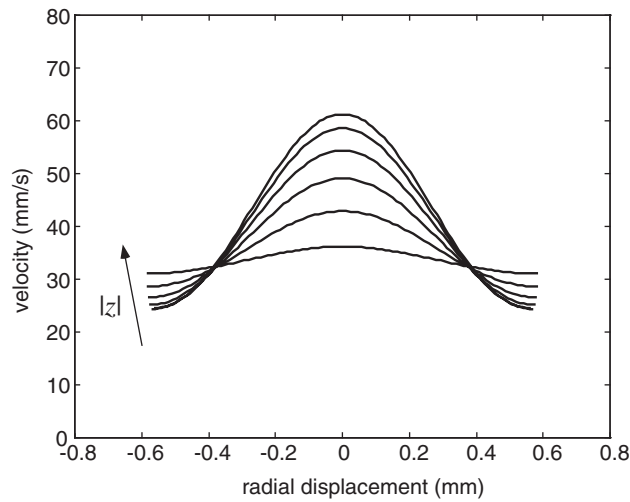
Figure 2. Calculated $v_z(r, z)$ versus r profiles across a tubeless siphon pertaining to the experiments reported here ($Q = 3.5 \times 10^{-8}$ m^2 s^{-1}, $\eta = 0.09$ Pa s, $\bar{\eta}_e = 60$ Pa s, $a_0 = 0.56$ mm, $h = 6$ mm) for $z = -0.5, -1.5, -2.5, -3.5, -4.5$ and -5.5 mm.

**Table 1.** Error terms from $\frac{\partial^2}{\partial z^2}$ associated with approximate solution of equation (2).

Term	Size
$A\bar{\eta}_e k\alpha' r J_0'(\alpha r) \exp(-kz)$	$\sim 10 \sqrt{\frac{\eta}{\bar{\eta}_e}} \frac{rz}{a^2} \rho g$
$A\bar{\eta}_e \alpha'^2 r^2 J_0''(\alpha r) \exp(-kz)$	$\ll \rho g$
$A\bar{\eta}_e \alpha'' r J_0'(\alpha r) \exp(-kz)$	$\sim \frac{r}{a} \rho g$

Table 1 shows the terms resulting from the spatial dependence of α. Terms arising from the spatial dependence of k are smaller by a factor of $\sqrt{\eta/\bar{\eta}_e}$ and will be neglected here.

Noting that $\bar{\eta}_e \gg \eta$, we expect the unwanted terms to be either of the order of the gravitational term, ρg, or smaller. This suggests that they are insignificant in the upper section of the column where shear stress dominates, but that they may become important near the column base. We will see in what follows that the extensional viscosity can be determined from velocimetry measurements, using the upper part of the column where shear effects predominate. In effect we obtain $\bar{\eta}_e$ by reference to η through the ratio $\eta/\bar{\eta}_e$ in equation (5). In the lower part of the column, where the gravitational term $\rho g/2\bar{\eta}_e$ plays a significant role, an absolute determination of $\bar{\eta}_e$ is, in principle, possible.

2.3. Calculated velocity profiles

Figure 2 shows a set of $v_z(r, z)$ versus r profiles calculated via equation (6) using parameters which apply in this work, and neglecting the effect of surface tension. In this example the value of A has been chosen to give a wall slip velocity of around 40% of the maximum velocity, $v_z(0, 0)$, at the entrance to the pipe. Note the gradual decrease in the shear down the column, and the zero-shear boundary conditions. Figure 3 shows corresponding $v_z(r, z)$ versus z profiles. In the lower part of the column, where the velocities at different radii converge,
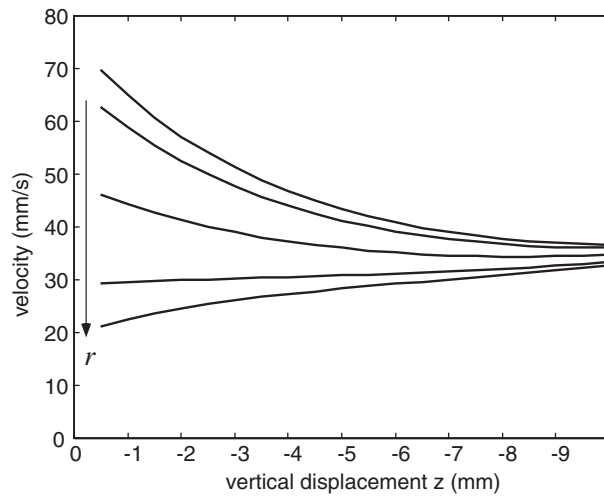
Figure 3. Calculated $v_z(r, z)$ versus z profiles across a tubeless siphon pertaining to the experiments reported here ($Q = 3.5 \times 10^{-8}$ m^2 s^{-1}, $\eta = 0.09$ Pa s, $\bar{\eta}_e = 60$ Pa s, $a_0 = 0.56$ mm, $h = 6$ mm) for $r = 0$, $a/4$, $a/2$, $3a/4$ and a.
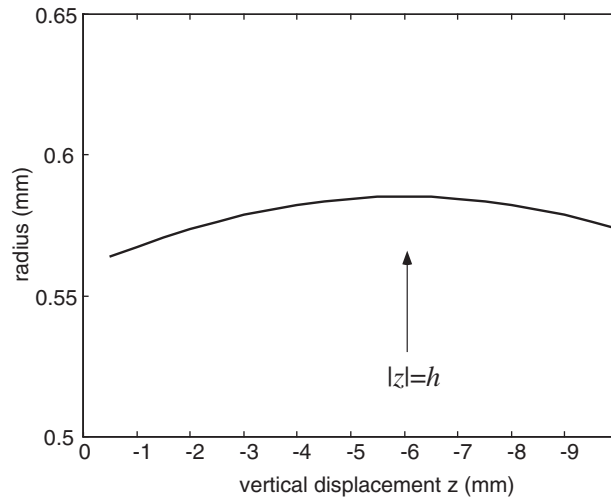

Figure 4. $a(z)$ versus z profiles calculated across a tubeless siphon pertaining to the experiments reported here.

the shear is significantly damped out. In this region the approximate solution becomes non-physical and error terms in equation (6) are significant. Figure 4 shows the $a(z)$ versus z profile, the maximum corresponding to the point of the velocity minimum, and below which the model breaks down.

3. Experimental details

The apparatus used for the tubeless siphon experiments is shown schematically in figure 5. It comprises a reservoir of diameter 12.5 mm and length 600 mm, into which is inserted a siphon pipe drawn from a glass Pasteur pipette. This pipe has an inner diameter of 1.2 mm and an
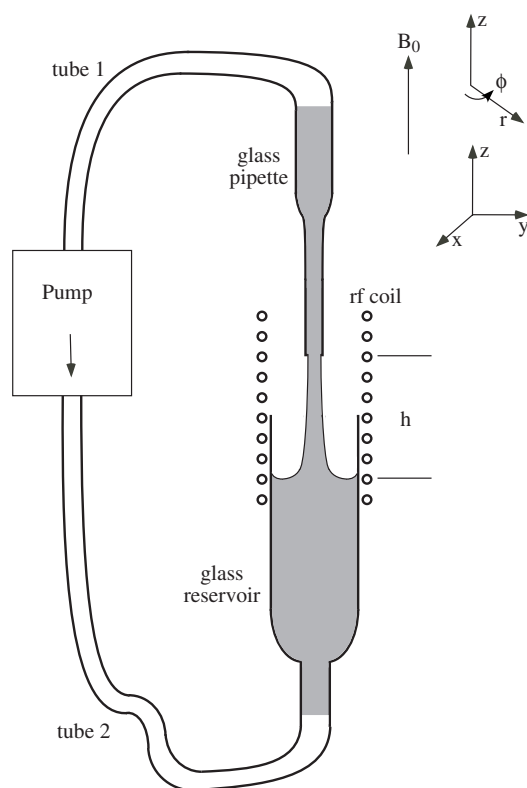
Figure 5. A schematic diagram showing the arrangement of the reservoir, inlet pipette and Fano column, inside the rf coil of the NMR system.

outer diameter of 1.7 mm. The siphon pipette and the reservoir inlets are connected via 6 m of 4 mm ID plastic tubing to the inlets and outlets respectively of a pump (Cole–Parmer model 72511-35). The system is filled with around 600 ml of 0.5% w/v 8×10^6 Da polyethylene oxide (Aldrich catalogue number 37 283-8) in water. The polymer solution was also doped with 0.1% $CuSO_4$ to reduce the spin–lattice relaxation time of the fluid. The flow curve (see figure 6) was measured using a Rheometrics RS5000 rheometer in a cylindrical Couette cell geometry and yielded a zero-shear viscosity of 0.09 Pa s.

The reservoir and pipette tip are located within the 15 mm diameter rf coil of an NMR microimaging system, within the bore of a 7 T superconducting magnet. Before the onset of flow, the tip of the glass siphon pipe is lowered into the polymer fluid in the reservoir and the pump started. Once steady state flow is established, the tip of the pipe is gradually lifted to a distance of several millimetres above the surface of the reservoir fluid, thus creating a tubeless column undergoing Fano flow. The flow rate, Q, was measured by NMR velocimetry to be 125(5) ml h^{-1}. Calibration of the NMR flow rate against the pump setting showed agreement to within the measurement precision. Repeated experiments showed that it was possible to establish a column height of up to 6 mm while retaining stable flow. Figure 7 shows a photograph of a stable tubeless fluid column taken while the apparatus was outside the magnet system.

A Bruker AMX300 spectrometer equipped with a 25 mm three-axis magnetic field gradient set was used for all microimaging experiments. The system utilized the 300 MHz proton NMR
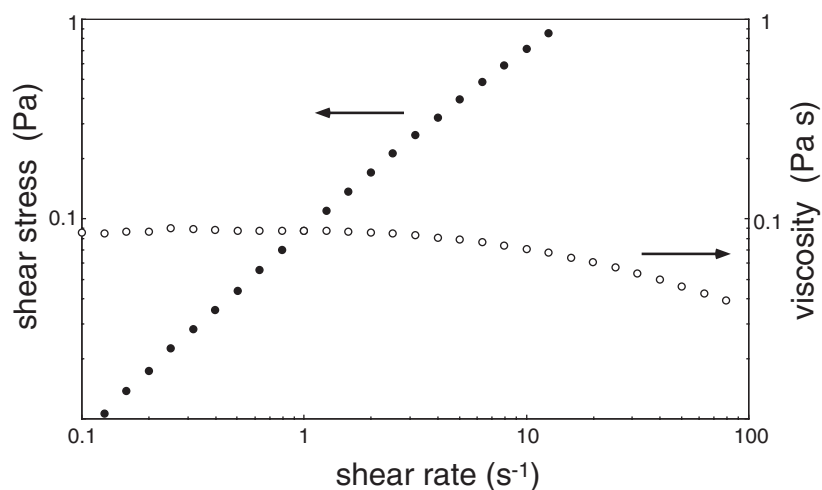
Figure 6. The flow curve for 0.5% w/v 8×10^6 Da polyethylene oxide in water.
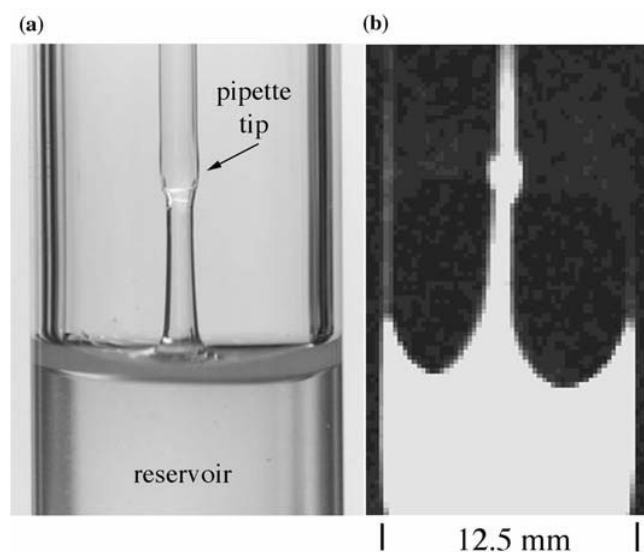
Figure 7. (a) A photograph of the tubeless siphon obtained under similar conditions to those used in the NMR velocimetry experiment. (b) A vertical section through the Fano column, pipe and reservoir taken at the start of the experiment reported here.

signal from the water molecules of the solution. Magnetic resonance imaging was used to observe the column, the pipe and the reservoir while they were in the magnet. The apparent discrepancy between the curvature exhibited in the optical and NMR images has two causes. First, the NMR image shows a section obtained in a vertical slice through the column while the optical image shows the projection. Second, in consequence, the true curvature of the column base was partially masked by the meniscus at the front and back of the column. Of course it was not possible to take a photograph while the siphon was inside the magnet and rf antenna during the NMR experiment. While we believe that partial masking is the principal reason for the discrepancy between the photograph and the image, we also note that the NMR image was

obtained after the initial photograph and it is possible that the reservoir liquid had changed shape once flow was established inside the NMR apparatus, although both the photograph and the NMR image were obtained under steady state flow conditions.

Some comment regarding the choice of reservoir diameter is necessary. The larger the reservoir diameter, the less the perturbing effect of curvature at the Fano column base; but equally, the larger the diameter of the rf coil needed to contain the reservoir, the smaller the signal-to-noise ratio and hence the poorer the spatial resolution of the NMR image. The reservoir diameter of 12.5 mm was a compromise, chosen so that the reservoir tube would fit inside a 15 mm rf resonator.

Velocity mapping was performed using a pulsed gradient spin echo (PGSE) NMR contrast scheme [16] along with a standard two-dimensional spin warp imaging sequence. Velocity images were obtained at various heights along the column, using a slice transverse to the column and with thickness 1 mm. The in-plane resolution was $31.25 \, \mu$m. Velocity analysis was based on the q-space Fourier transform method [16, 17] using eight q-encodings comprising gradient pulses of duration $\delta = 1$ ms, separation $\Delta = 5$ ms and maximum gradient 0.21 T m^{-1}. Note that the velocity determination using this method does not require a narrow gradient pulse and is exact irrespective of the ratio δ/Δ. The accuracy of the method is determined by frequency domain calibrations of the gradient strength and is better than 1%. The precision of the method is limited by a combination of pixel signal-to-noise ratio and the molecular Brownian motion over the timescale Δ. We estimate this precision to be between 1 and 3% for the velocity range studied here. It should be noted that the PGSE q-encoding contrast scheme has proved highly effective at measuring flows in a geometry in which the radius of the pipe is changing. In particular, Xia *et al* [18] have shown precise agreement between NMR velocimetry and finite element model solutions to the Navier–Stokes equations for flow near an abrupt contraction.

A large number of experiments were performed in order to obtain a data set in which the flow was stable over the 4 h needed to obtain a complete set of 16 velocity maps over the entire column and in the pipe entrance region. In some experiments the column broke during the run, or slowly migrated across the reservoir surface. The data shown in this paper belong to a single run in which stable conditions obtained throughout the flow. These data are representative of all experiments performed under stable column conditions. We were able to ascertain that the column was indeed stable by imaging the vertical section of the column at regular intervals.

4. Results

In order to ascertain the location of the Fano column within the rf coil, a series of NMR images are obtained. These provide a 'proton density map', essentially a map of water density. The right-hand side of figure 7 shows a vertical section taken through the column once stable tubeless siphon flow was established. The slice thickness in the image is 1 mm. Note the fluid around the outside of the glass pipette, near the entrance. This wetting layer arises from the initial insertion of the pipette into the reservoir fluid. The base of the Fano column exhibits strong curvature which continues across the top of the reservoir fluid right to the reservoir wall, a behaviour which is maintained throughout the 4 h course of the velocimetry measurements. This curvature is a feature of our experiment and is presumably associated with our use of a small diameter reservoir in the limited space available within the rf coil. One possible explanation for the curvature is that it allows surface tension to balance the small pressure difference across the air/fluid interface associated with Bernoulli effects. Given a surface tension of water of around 0.07 N m^{-1} (assuming that this is little modified by the 0.5% polymer solute) and allowing for flow towards the siphon, we find that Bernoulli effects are far too weak to account for the observed curvature of around 200 m^{-1}. We suggest that the
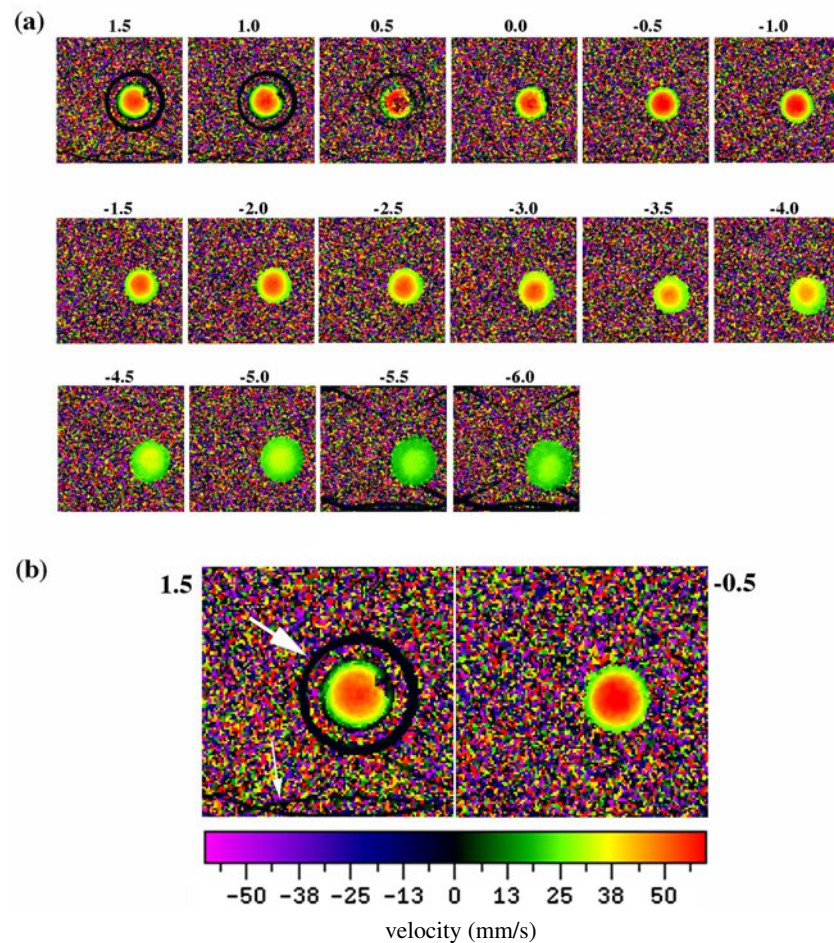
Figure 8. (a) Velocity maps obtained at various heights using horizontal sections of 1 mm thickness. Negative values of z refer to sections below the pipe entrance. Noise corresponds to an absence of fluid while dark regions arise from stationary fluid. (b) Expanded velocity images for the positions $z = -0.5$ and 1.5 mm. The arrows indicate stationary fluid wetting the outer surface of the pipette (large arrow) and due to 'foldbacks' from the fluid wetting the inner surface of the reservoir tube (small arrow).

behaviour at the base of the column reflects an interplay of surface tension, shear stress and extensional stress effects, with the latter playing an important role.

Figure 8(a) shows a series of velocity maps obtained at various heights in the flow field. The noise corresponds to regions where the proton density is zero (i.e. fluid is absent). Note that the flow is not perfectly symmetric. Curiously, the more rapidly moving fluid core winds about during the transit of fluid up the column. Note the dark streaks which appear at $z = -5.5$ mm and below. These arise from stationary fluid on the inner wall of the reservoir, fluid which is outside the field of view and whose appearance is due to Nyquist foldback.

Figure 8(b) shows expanded velocity images for the positions $z = -0.5$ mm (in the Fano column just below the pipe entrance) and $z = 1.5$ mm (a short distance inside the pipe). The dark ring surrounding the region of finite fluid velocity in the latter image arises from stationary
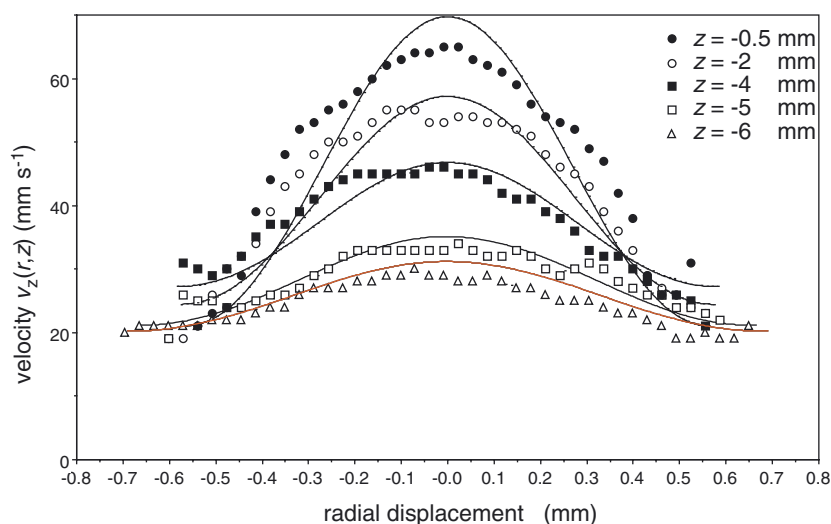
Figure 9. Measured $v_z(r, z)$ versus r profiles at $z = -0.5, -2, -4, -5$ and -6 mm. These are compared with those calculated (solid curves) using equation (6) using the parameters $Q = 3.5 \times 10^{-8}$ m^2 s^{-1}, $\eta = 0.09$ Pa s, $\bar{\eta}_e = 60$ Pa s, $a_0 = 0.56$ mm, $h = 6$ mm. A is chosen to match the pipe inlet wall slip ($z = 0$). In the case of $z = -5$ and -6 mm the experimental column radii are used in the calculation of $v_z(r, z)$. Note that the profiles have been centred, correcting for the offsets associated with the slight column slant, as is apparent in figure 8.

fluid which is wetting the outside of the pipe. The contrast between the Fano column velocity image at $z = -0.5$ mm and the pipe fluid velocity image at $z = 1.5$ mm is interesting in two respects. First, we note that the diameter of the column just below the entrance is slightly less than that in the pipe ID. Second, we see that by $z = 1.5$ mm, a non-slip boundary condition is nearly established (see the dark $v_z(a, z) \approx 0$ boundary) whereas just below the entrance a distinct non-zero velocity is observed at $r = a_0$.

In order to compare the velocity maps with the predictions of the model, we have taken a number of representative one-dimensional profiles of $v_z(r, z)$. In the case of fixed z, five representative profiles of $v_z(r, z)$ versus r were obtained at $z = -0.5, -2, -4, -5$ and -6 mm. In each case a transverse velocity profile was taken from the images shown in figure 8(a). These are shown in figure 9. Note the asymmetry of the profile for the case of $z = -4$ mm, associated with the flow asymmetry apparent in the $z = -4$ mm image shown in figure 8(a). This asymmetry may well be a consequence of the slight 'slant' in the column, obvious from inspection of the images in figure 8(a). For the analysis of $v_z(r, z)$ versus z behaviour, as seen in figure 10, we average velocity values obtained at four points on a quadrant at each of $r = 0$, $r = a/2$ and a using each of the 0.5 mm spaced images shown in figure 8(a). Finally, in figure 11 we show the Fano column radii $a(z)$ measured from the proton density maps associated with each image of figure 8(a). Also shown are two data points for fluid within the pipe ($z > 0$). The slight 'necking' of the fluid prior to the entrance (at $z > -0.5$) is apparent in figure 11. For this reason we have chosen to use, as our highest level in the analysis, the profile at $z = -0.5$. Note that the integrated flow rates obtained by summing the velocities measured for all pixels in the five representative cross sections are respectively 3.7, 3.8, 3.5, 3.1 and 3.3×10^{-8} m^3 s^{-1}, a variation which largely arises from digitization effects associated with the finite number of pixels across the column.
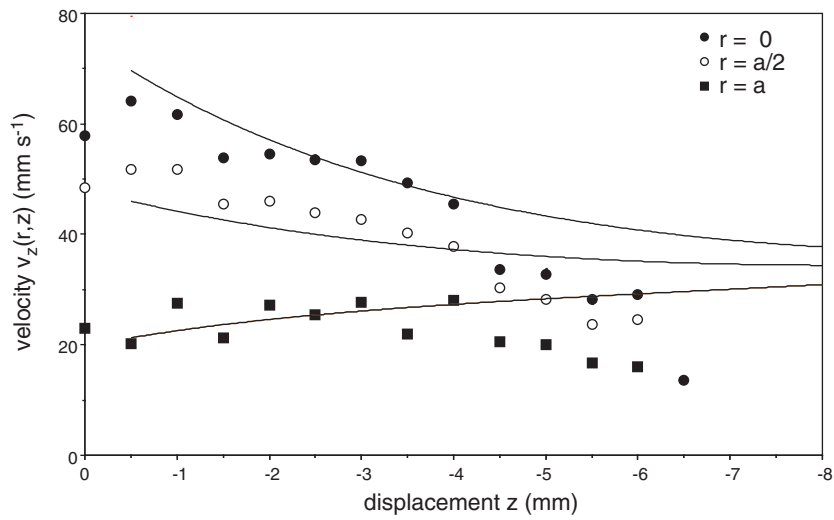
Figure 10. Measured $v_z(r, z)$ versus z profiles compared with those calculated using equation (6) with the parameters of figure 9.
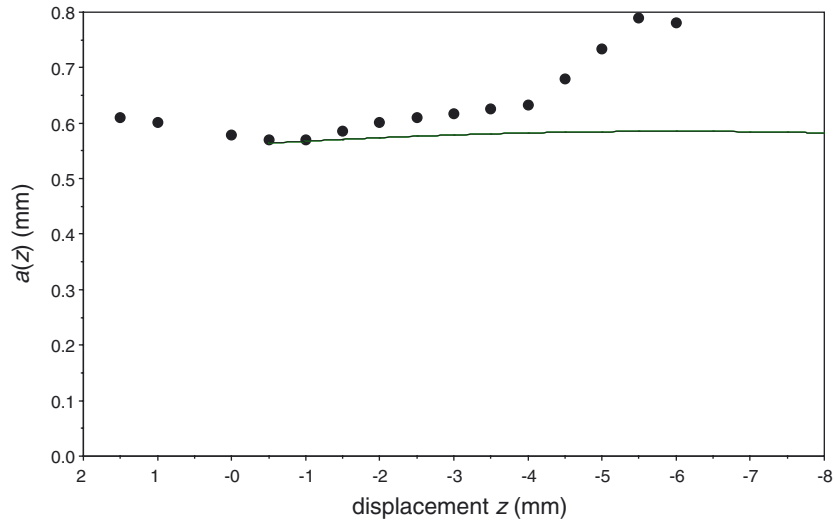
Figure 11. A measured $a(z)$ versus z profile compared with that calculated using the simple model based on equation (8) with the parameters of figure 9.

5. Discussion

In applying the model represented by equation (6) we first attempt a solution based on the zero-shear-rate boundary condition associated with setting $\gamma \approx 0$. First we average the integrated flow across the pipe to obtain the flow rate $Q = 3.5 \times 10^{-8} \text{ m}^3 \text{ s}^{-1}$. Next we fix the value of h to 6 mm, the height of the column, and a_0 to 0.56 mm, the observed radius at $z = -0.5$ mm. Shear rates within the column range from a few s^{-1} to around 100 s^{-1} and this begs the question as to the appropriate choice of shear viscosity. However, η varies by only a factor of two over this range, and we choose the low shear plateau value of 0.09 Pa s which apples for most of the shear rates encountered in the column. We note however that any lower choice would similarly

reduce the estimated value of $\bar{\eta}_e$. With these various parameters fixed, and with a choice of the fit parameter $\bar{\eta}_e$, constants C and B are calculated using equations (4) and (7), while $a(z)$ (and hence α) can be calculated using equation (8). Finally, a value of A is chosen, between 0 and $Q/\pi a_0^2 J_0(\alpha a_0)$, which allows a match to the fluid velocity of the exterior of the Fano column at $z = -0.5$ mm. In the present case we find a good match to this boundary condition with $A = 0.45/\pi a_0^2 J_0(\alpha a_0)$.

Figures 9 and 10 show the comparison between theory (solid curves) and the measured velocity profiles. In the adjustment of $\bar{\eta}_e$ to provide a fit, it was noticed that the data from the longitudinal profiles provide the most sensitive test. This test is applied in effect through the variation of k via equation (5). In particular we note that the postulated $\exp(-kz)$ profile at the column centre, $v_z(0, z)$, versus z is not particularly well represented by the data for $|z| < 5$ mm. Furthermore, the radial profiles show quite distinct deviations from a simple Bessel shape near the entrance. The inflected profiles may be due to variations in the diameter of the fluid column associated with the effects of surface tension between the fluid and the glass pipette tip.

Figure 11 shows the column radii calculated using equation (8). The calculated slope $|\partial a(z)/\partial z|$ is smaller than that observed. Furthermore there is a considerable broadening of the column below $z = -4.5$ mm. In order to properly represent the velocity profiles corresponding to $|z| \geqslant 5$ mm, it is necessary to use these experimental radii in that region. The calculated $v_z(0, z)$ versus r profiles at $z = -5$ and -6 mm are so obtained, using all other parameters common to the set for $|z| < 5$ mm, and with only the column radius changed. The resulting match to the data shown in figure 9 is excellent. By contrast figure 10 shows $v_z(0, z)$ versus z profiles in which the calculated $a(z)$ values are used throughout. Not surprisingly, increasing the column radius in the vicinity, $|z| \geqslant 5$ mm, improves the match to the data.

We now address the question as to whether effects of surface tension between the fluid and the air surface can be reasonably neglected in setting the boundary conditions at $r = a$. From equation (9) we can calculate the expected velocity gradient at the surface, in the region of the column $|z| < 5$ mm. Using the zero-shear value for $\eta = 0.09$ Pa s, $\gamma = 0.07$ N m^{-1}, $a = 0.5$ mm and our measured value of $\partial a(z)/\partial z \approx 0.01$, we find $\partial v_z/\partial r \approx 10$ s^{-1} at the surface. Note that in retrospect, this value of shear rate slightly displaces the viscosity to the shear thinning region, but the initial choice of zero-shear value is sufficiently close that our rough estimate of the surface shear rate is reasonable. Given the value of A needed to fit the $v_z(r, z)$ versus r profile near the entrance, and using α of the order of $3.8317/a$, we find from equation (10) that at the surface $J_1(\alpha a) \approx 0.06$ rather than zero. This yields a corrected value of $\alpha \approx 3.68/a$, sufficiently close to the root that we may justifiably neglect surface tension induced boundary shear. Note that the calculated value of $\partial v_z/\partial r \approx 10$ s^{-1} is in accord with the data shown in figure 9 and is at least an order of magnitude smaller than strain rates found nearer the centre of the flow.

At the flow rate used in this work, the dominant role of the extensional stress in the upper part of the Fano column is in balancing the shear stresses. Only in the lower section of the column, where shear effects are less important, does the gravitational pressure gradient play a dominant role. Furthermore, the lower the flow rate used, the more gravitational influences become important in determining the first-order velocity field throughout the column. Clearly any exact solution must reflect a smooth change from the shear-dominant region to the gravitational region and, to that extent, our model is deficient.

In our model, the average velocity in the upper part of the column is given by equations (7) and (11) as

$$\langle v_z \rangle = \frac{Q}{\pi a_0^2} + Cz^2 + 2Chz. \tag{12}$$

This quadratic dependence is apparent in the data of many other studies [19, 20, 5, 7, 21] although these authors often assume, for convenience, a linear dependence of v_z on z [9]. In each of these studies a strong deviation from quadratic behaviour is seen at the base of the column where column bulging is apparent. It is for precisely this region that our assumptions are weak and that we are least confident about our predictions. Remarkably however, we do find a reasonable match between our $v_z(r, z)$ versus r predictions and the profiles measured at the base of the column, once the observed radius anomaly is incorporated.

In the high flow case, the nearly $\exp(-kz)$ dependence of the central velocity down the column provides an effective means of determining $\bar{\eta}_e$, via equation (5) and the relation $\alpha(z) = 3.8317/a(z)$. Finally, we note that the value of the extensional viscosity obtained in this work by fitting the observed velocity field is $\bar{\eta}_e \approx 60$ Pa s, at an average extensional strain rate of around $10 \, \text{s}^{-1}$. The error in this value is estimated at around 20 Pa s, based on the fitting sensitivity and the uncertainty in the effective shear viscosity over the wide range of shear rates experienced by the column. This value of $\bar{\eta}_e \approx 60$ Pa s is similar to that obtained for comparable polyethylene oxide solutions at similar strain rates. In particular we note that Gauri and Koelling [22] obtained 40 Pa s for a 1.5% w/v water solution of 4×10^6 Da polyethylene oxide, independent of strain rate over two decades. Scaling for the higher molar mass, and lower concentration in the present case, the value of 60 Pa s seems reasonable.

6. Conclusion

Fano flow is most easily established in fluid columns of small ($\sim$mm) radial extent, where the high strain rates needed can be achieved using realistic flow rates, Q. In consequence, any method used to measure the interior velocity field will require microscopic resolution. The velocity images presented here, to our knowledge the most detailed yet available, suggest that NMR microscopy is a powerful tool in such studies. These images provide detailed insight regarding the Eulerian velocity field within the Fano column and have allowed us to test a simple model for Fano flow. This model, which is based on a simple differential equation for $v_z(r, t)$, coupled with an imposed continuity condition, has an approximate closed form analytic solution which provides a useful approach, to first order, in the upper part of the column. The solution is amenable to simple boundary conditions and has only two fitting parameters, one of which is free, while the other is determined by the velocity field observed at the entrance to the pipe.

An intriguing aspect of our observations is that shear stresses dominate the gravitational stress in the upper region of the column. Whether a Fano column without shear can be sustained is subject to conjecture, but on the basis of our results we suggest that the transition to gravitational dominance at the base of the column may herald the onset of instability and column breakage. The anomalous radius of the column near the reservoir surface suggests a transition in the physics. The fluid behaviour at the column base remains a matter of conjecture and should be an ideal subject for future NMR velocimetry studies, especially given the difficulty of using optical techniques near the reservoir surface.

Our results suggest that NMR velocimetry, when performed with microscopic resolution, provides a means of effectively determining the ratio $\eta/\bar{\eta}_e$, and hence enables measurement of extensional viscosities under steady state flow conditions. We further suggest that many unresolved details of Fano flow might be elucidated using the methods outlined in this paper.

Acknowledgments

References

[1] Xia Y and Callaghan P T 2003 *J. Magn. Reson.* **16** 365
[2] Fano G 1908 *Archiv. Fisol.* **5** 365
[3] Larson R G 1999 *The Structure and Rheology of Complex Fluids* (New York: Oxford University Press)
[4] Balmer R T 1977 *J. Non-Newton. Fluid Mech.* **2** 307
[5] Balmer R T and Hochschild D J 1978 *J. Rheol.* **22** 165
[6] Macsporran M C 1981 *J. Non-Newton. Fluid Mech.* **8** 119
[7] Otsubo Y and Umeya K 1982 *J. Appl. Polym. Sci.* **27** 1655
[8] Acierno D, Titomalio G and Nicodemo L 1974 *Rheol. Acta* **13** 532
[9] Peng S T J and Landel R F 1976 *J. Appl. Phys.* **47** 4255
[10] Chao K K and Williams M C 1983 *J. Rheol.* **27** 451
[11] Matthys E 1988 *J. Rheol.* **32** 773
[12] Fuller G G, Cathey C A, Hubbard B and Zebrowski B E 1987 *J. Rheol.* **31** 235
[13] Fuller G G and Leal L G 1980 *Rheol. Acta* **19** 580
[14] Fuller G G and Leal L G 1981 *J. Polym. Sci. Polym. Phys.* **19** 557
[15] Sridhar T, Tirtaatmadja V, Nguyen D A and Gupta R K 1991 *J. Non-Newton. Mech.* **40** 271
[16] Callaghan P T 1993 *Principles of Nuclear Magnetic Resonance Microscopy* (New York: Oxford University Press)
[17] Callaghan P T 1993 *Rep. Prog. Phys.* **62** 599
[18] Xia Y, Jeffrey K R and Callaghan P T 1992 *AIChE J.* **38** 1408
[19] Astarita G and Nicodemo L 1971 *Chem. Eng. J.* **1** 57
[20] Nicodemo L, De Cindio B and Nicolais L 1975 *Polym. Eng. Sci.* **15** 679
[21] Otsubo Y and Umeya K 1984 *J. Appl. Polym. Sci.* **29** 1467
[22] Gauri V and Koelling K W 1997 *Rheol. Acta* **36** 555